Numerical simulation of pollutant dispersion characteristics in a three-dimensional urban traffic system

Hongwen Dou[a], Tingzhen Ming[a,*], Zhengtong Li[b], Chong Peng[c,*], Chen Zhang[c], Xinyu Fu[d]

[a] School of Civil Engineering and Architecture, Wuhan University of Technology, No.122 Luoshi Road, Hongshan District, Wuhan 430070, PR China
[b] School of Energy and Power Engineering, Huazhong University of Science and Technology, No.1037, Luoyu Road, Hongshan District, Wuhan 430074, PR China
[c] School of Architecture and Urban Planning, Huazhong University of Science and Technology, No.1037, Luoyu Road, Hongshan District, Wuhan 430074, PR China
[d] Department of Urban and Regional Planning, University of Florida, Gainesville, FL 32607, USA

ARTICLE INFO

ABSTRACT

A complex three-dimensional (3D) urban traffic system containing roundabouts and tunnels continues to emerge in China's metropolises. Based on this, a mathematical model was established to describe the fluid flow and CO propagation characteristics in a complex 3D traffic system, including a sunken bus stop area, traffic roundabout, viaducts, and tunnels. Features of pollution dispersion in those locations were analyzed under different ambient crosswinds (ACWs). The results showed that the distribution of pollutants in the 3D traffic system was greatly influenced by geometric parameters and their relative positional relationship. Distribution of pollutants in the 3D traffic system is rather complicated and varied. At a sunken bus stop area, changes in ambient wind will cause fluctuating pollution levels upstream and downstream at the bus stop, and symmetrical distribution has been exhibited under parallel wind. The effects of complex road conditions on pollutants are beyond the prevailing winds at the traffic roundabout. In a naturally ventilated municipal double-hole traffic tunnel, contaminants accumulate along the downstream direction, which is more pronounced at low wind speeds. However, dilution effects are enhanced in tunnels' open areas.

1. Introduction

With the rapid growth of China's economy and urbanization, the prevalence of motorized vehicles is gradually increasing. Automobile emissions not only cause the global greenhouse effect (De_Richter et al., 2017) but also impact urban air quality. In fact, vehicle emissions have become one of the most important pollutant sources in the city environment (Liu et al., 2008; Shahbazi et al., 2016), affecting humans' respiratory system, cardiovascular system, and nervous system (Lu et al., 2017; Mcdonald et al., 2004). Consequently, the issue of city traffic pollution has aroused widespread concern.

Several studies have been conducted on pollutant diffusion in idealized urban area models with certain geometrical structures (Krecl et al., 2015; Sabatino et al., 2013; Scungio, 2013; Tsai and Chen, 2004). Previously, scholars believed that ACWs perpendicular to the street exacerbated contaminant spread, and the geometry of roofs and aspect ratio of street canyons had a great influence on vortices (Kastner-Klein and Plate, 1999). Soulhac et al. (2009) investigated pollutant dispersion in a street canyon with road intersection. The results showed that a vortex formed at the beginning of the street, which determined the

exchange of pollutants between the street and the intersection; the level of pollutants ranged between a limited long street and an infinite street. Research about traffic roundabout showed that the effect of the complex relationship of road connections on pollutant dispersion went beyond prevalent ambient wind (Pandian et al., 2011).

In addition the above, studies about other aspects of this field have also attracted considerable attention. Firstly, several new simulation models have utilized flourishes, including the first-tested detached eddy simulation (DES) model (Scungio et al., 2015a), which was found to be sufficiently accurate; and the one-equation Spalart-Allmaras turbulence model (Scungio, 2013). Secondly, particle dispersion has piqued researchers' interest (Scungio et al., 2015b; Zhang et al., 2011). Thirdly, measures aimed at improving air quality in street canyons have been developed. Moradpour et al. investigated the effects of green roofs (Moradpour et al., 2017) and urban vegetation design (Moradpour et al., 2016) on the outdoor thermal environment and pollutant levels; both were proved to be effective environmental improvement strategies.

With the rapid development of urbanization in China and the growing size of cities, more 3D traffic systems are being constructed to

Please cite this article as: Dou, H., Atmospheric Pollution Research (2018), https://doi.org/10.1016/j.apr.2018.01.018

(a)
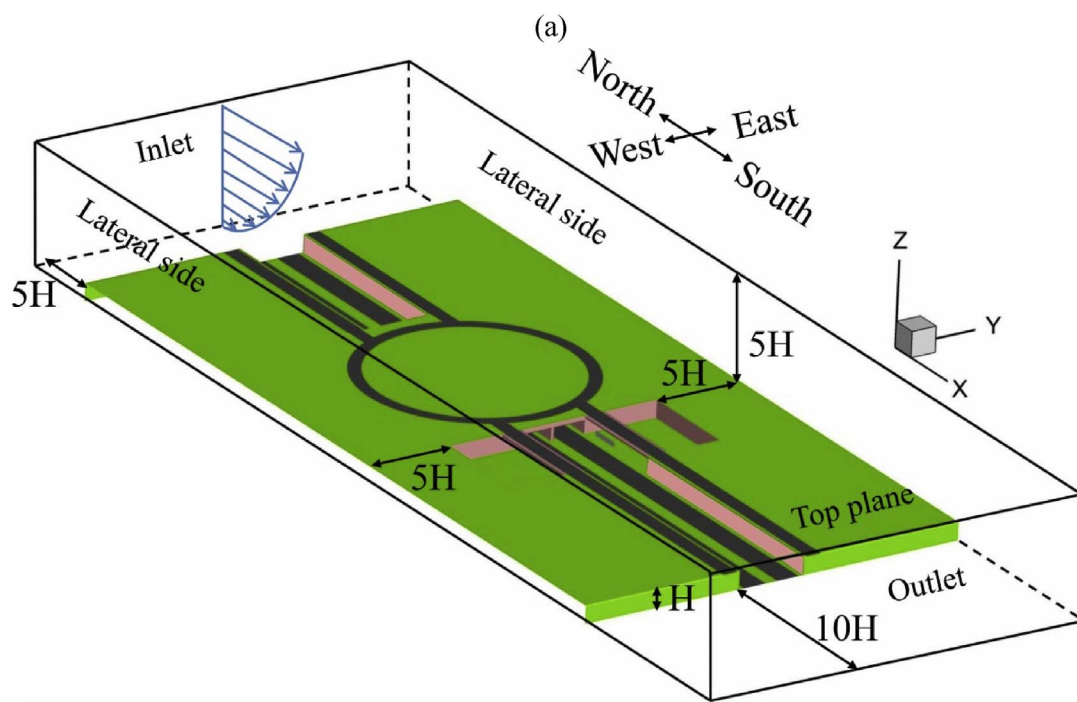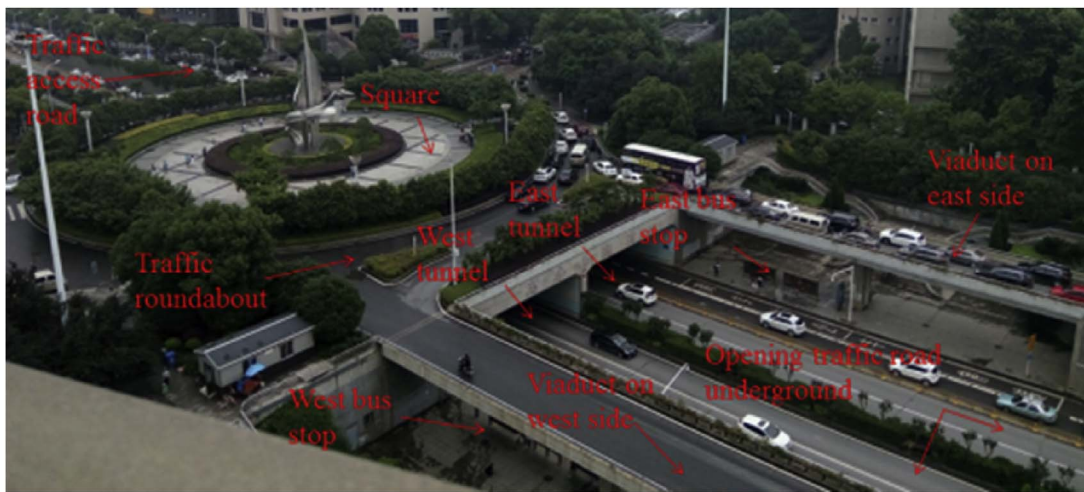
(b)
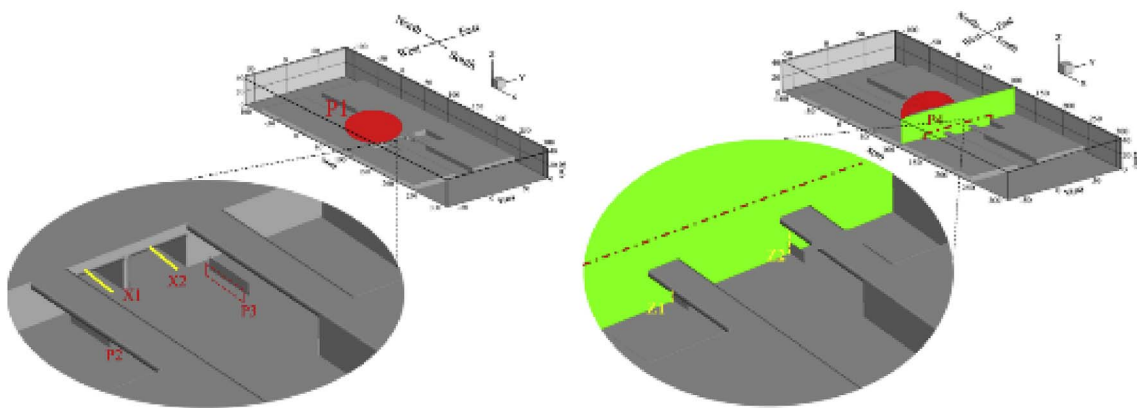
(c)

(d)

Fig. 1. Real and physical model: (a) the real 3D traffic system contains three major research objects: the bus stop area, the traffic roundabout, and the tunnels; (b) physical model; (c) position of the object region of planes P1, P2, and P3 and lines X1 and X2 in the physical model; (d) position of the object region of plane P4 and lines Z1 and Z2 in the physical model.

alleviate traffic pressure. Current studies on pollutant dispersion in three-dimensional traffic have considered pollutant dispersion in streets with viaducts (Hang et al., 2016). Results have shown that viaducts (especially those with soundproof walls) significantly reduce the concentration of gas pollutants within buildings above the viaduct. Due to the complexity of the three-dimensional traffic system and the time-consuming nature of numerical calculations, the three-dimensional traffic system is generally simplified into a 2D geometric model (Hang et al., 2016; Lin et al., 2014). The 2D model predicts that fresh air flowing into the street is much less because there is no current coming from the sides of the canyon. Therefore, contaminant migration can only flow through the street canyon's upper opening, thus increasing the level of pollutants in the street. Compared to the actual street, these results exhibit large variability (Tsai and Chen, 2004). In addition, the model for three-dimensional traffic is also limited to streets with viaducts, and research on other geometric features has not received much attention.

This paper presents a 3D traffic model with an annular intersection, viaduct, sunken bus stop area, and tunnels (Fig. 1) according to a real road in Wuhan, China. These structures often provide both the inhabitant's places of activity and traffic lanes which makes it be very popular in modern cities. There are over 50 similar structures in Wuhan according to a survey (National Bureau of Statistics of China, 2017). Thus, researches about these kind structures are vital as air flow and pollutant dispersion characteristics have not ever been reported previously. Usually, these structures have the following characters: Firstly, the intersection of the annular road in the model differs from typical crossroads. The traffic roundabout generally does not contain traffic signal lights, and vehicles move continuously. The spread of pollutants is different from traditional road intersections (Gokhale and Patil, 2010; Pandian et al., 2011; Soulhac et al., 2009). Secondly, the upper zone of the bus stop is affected by the viaduct, which is located in a sunken area. Finally, for the natural ventilated double-hole tunnel, pollutant diffusion is dramatically affected by geometric structures at the north and south tunnel openings. The CFD method was used to study pollutants' propagation characteristics in this type of three-dimensional traffic system.

2. Model description

2.1. Physical model

A three-dimensional model is shown in Fig. 1 to investigate the propagation characteristics of gaseous pollutants, where the X-axis originates from north to south and the Y-axis originates from west to east. The model contains the following areas: a double-hole traffic tunnel (DHTT), sunken bus stop area with western and eastern bus stop boards, viaduct, and square on the ground. The board has a height of 2 m and is 0.5 m from the ground and 3.5 m from the viaduct. The two boards are located 2 m from the lane, as shown in Fig. 1(a). The radius of the inner circle of the traffic roundabout is 40 m, and that of the outer circle is 45 m. The traffic system has a height of H, and H = 7 m. According to the study of Solazzoet al. (Solazzo et al., 2008), the distance to the traffic structure can be set as 5 H (to eliminate the influence of velocity inlet on the flow field distribution). Table 1 shows the boundary condition of the domain.

Table 1
Boundary condition of the physical model.

Surface	Boundary type	Distance from the traffic system
Inlet	Velocity_inlet	5H
Lateral side	Symmetry	5H
Top plane		
Outlet	Pressure_outlet	10H

All the traffic lanes in Fig. 1(a) were abstracted as pollutant sources, namely the grey stripes and circle in Fig. 1(b). Fig. 1(c) shows the P1 plane, which actually contains a square and the traffic roundabout with a radius of 45 m. X1 and X2 lines are located in the center of the two tunnels, respectively, stretching through the entire tunnel with a length of 100 m. P2 and P3 planes that are 1 m away from the corresponding bus stops have the same size of bus brands. Fig. 1(d) shows the P4 plane, which crosses the middle of the bus brand. Z1 and Z2 lines stretch from the ground to the bottom of viaduct.

2.2. Mathematical model and calculation process

In this paper, the renormalization group (RNG) k-ε model was utilized to calculate the turbulent flow in the complex domain, which was proved by many researchers to be appropriate and sufficiently accurate to solve cases of this kind (Konstantinov et al., 1998; Tsai and Chen, 2004). It corrected turbulent viscosity and considered the swirling and swirl flow within the average flow (Long, 2007). Therefore, the RNG k-ε model could better solve the flow containing a high strain rate and flow line with a greater bending degree (Konstantinov et al., 1998; Raw et al., 1989).

There are some assumptions made in this model to perform calculations:

(a) Fluid flow in the domain is continuous and incompressible;
(b) There are no chemical reaction processes in this research;
(c) Given that most days of the year in Wuhan are either cloudy or overcast, radiation effects and heat transfer are not considered;
(d) Traffic congestion often occurs on such a busy road, especially during the morning and afternoon rush hours, when vehicles move rather slowly. This study focuses on the time period when traffic turbulence is too weak to be considered;
(e) Traffic congestion often continues for a long time, during which airflow and contaminant spread are steady.

Thus, the governing equations including Mass, Navier-Stokes, and RNG k-ε turbulence model can be written as follows:.

Mass equation:

$$\frac{\partial(u_i)}{\partial x_i} = 0 \tag{1}$$

Navier–Stokes equation:

$$\frac{\partial(\rho u_i u_j)}{\partial x_j} = \rho f_i - \frac{\partial p}{\partial x_i} + \frac{\partial}{\partial x_j}\left[\mu\frac{\partial u_i}{\partial x_j} - \rho\overline{u_i' u_j'}\right] \tag{2}$$

In the above equation, u_i represents the average flow velocity, u_i' represents the pulse value, ρ represents the fluid density, and μ represents the kinematic viscosity.

The average Reynolds stress $\overline{u_i' u_j'}$ can be expressed as

$$\overline{u_i' u_j'} = -v_t\left(\frac{\partial u_i}{\partial x_j} + \frac{\partial u_j}{\partial x_i}\right) \tag{3}$$

The kinetic energy k equation is

$$\frac{\partial(\rho \kappa u_i)}{\partial x_i} = \frac{\partial}{\partial x_j}\left(\alpha_\kappa \mu_{eff}\frac{\partial \kappa}{\partial x_j}\right) + G_k + \rho\varepsilon \tag{4}$$

The turbulence dissipation rate ε equation is

$$\frac{\partial(\rho\varepsilon u_i)}{\partial x_i} = \frac{\partial}{\partial x_j}\left(\alpha_\varepsilon \mu_{eff}\frac{\partial \varepsilon}{\partial x_j}\right) + \frac{c_{1\varepsilon}^*\varepsilon}{\kappa} - G_\kappa - C_2\varepsilon\rho\frac{\varepsilon^2}{\kappa} \tag{5}$$

In the above equation,

$$\mu_{eff} = \mu + \mu_t \tag{6}$$

$$\mu_t = \rho C_\mu = \frac{\kappa^2}{\varepsilon} \tag{7}$$

$$C_{1\varepsilon}^* = C_{1\varepsilon} - \frac{\eta\left(1 - \frac{\eta}{\eta_0}\right)}{1 + \beta\eta^3} \tag{8}$$

In addition, the constant values used in (4)–(8) were, respectively,

$C_\mu = 0.0845$, $a_k = a_\varepsilon = 1.39$, $C_{1e} = 1.42$, $C_{2e} = 1.68$, $\eta_0 = 4.377$, $\beta = 0.012$

The pollutant transport equation was

$$\frac{\partial(\rho u_i c_s)}{\partial x_i} = \frac{\partial}{\partial x}\left(D_s \frac{\partial(\rho c_s)}{\partial x_i}\right) + S_s \tag{9}$$

where C_S represents the volume concentration of component S, D_S represents the diffusion coefficient of the component, and S_S represents the mass of the component produced per unit volume per unit time in the system. Among them,

$$D_s = -\frac{j_s}{\frac{d\rho_s}{d_i}} \tag{10}$$

where j_s is mass diffusion flux (Cussler, 1986) of component S in the air; the value is 1×10^{-5} m^2/s.

The numerical calculation was performed in Ansys Fluent 14.0. The pressure-velocity coupling was solved using the semi-implicit method for pressure-linked equations (SIMPLE) procedure (Patankar, 1980), and the iterative selection of the discrete equation was Green-Gauss node-based. The convergence criteria for each control volume were that the maximum residuals of the mass, momentum, and species were all below 1×10^{-5}.

2.3. Boundary conditions

Boundary conditions used in this paper are shown in Table 1. Firstly, the vertical velocity component of the velocity entrance was 0 under all conditions. Secondly, the angle between the ambient wind direction and the positive X-axis was defined as θ; therefore, θ = 0° represents north wind; θ = 180° denotes the south wind.

(1) Velocity inlet

The ambient crosswind (ACW) was set as a non-uniform vertical profile in the approach flow and described by the power law (Richards and Hoxey, 1993; Richards and Norris, 2011).

$$U_z = U_{ref}\left(\frac{z}{7}\right)^{0.2} \tag{11}$$

where U_{ref} is the reference velocity of ACW at a height of 7 m. The corresponding turbulent kinetic energy k and dissipation rate ε on the inlet surface are, respectively,

$$k = \frac{U_*^2}{\sqrt{C_\mu}} \tag{12}$$

$$\varepsilon = \frac{U_*^3}{\kappa z} \tag{13}$$

where $U_* = 0.54$ represents the friction velocity. $\kappa = 0.41$ is the von Karman constant.

In this study, the ACW was set to five directions, namely θ = 0°, θ = 45°, θ = 90°, θ = 135°, and θ = 180° under the condition of $U_{ref} = 2.0$ m/s. Moreover, three other U_{ref} were also considered when studying the effects of ACW velocity, respectively: $U_{ref} = 0.5$ m/s, $U_{ref} = 1.0$ m/s, and $U_{ref} = 1.5$ m/s, assuming θ = 90°.

(2) Symmetry

According to the results of Solazzo et al. (2008), the flow on the lateral and top surfaces of the domain can be considered symmetric where the normal gradient is 0 (FLUENT, 2006).

2.4. Pollutant source

In this study, CO was used as the tracing gas of vehicle emissions. For the intensity of pollution sources C_p, the actual value should be estimated by vehicle emissions; therefore, the value varies based on real vehicle emission standards, car type, engine speed, fuel quality, and other factors (Tang et al., 2003). Tsai and Chen (2004) provided its specific value via measurement and relative computation considering the effects of light-duty vehicles, heavy-duty vehicles, and traffic flow rate. Given that a similar circumstance between the research area of our target city and Tsai's, we referred to his value, $C_p = 4 \times 10^{-6}$ Kg/m^3.

2.5. Meshing skill and grid independence

A structural grid has the advantages of easily realized boundary fitting in the region, high-speed grid generation, and a simple data structure; hence, we adopted the grid in our mesh system. The entire sunken bus stop area, tunnels, and the areas near walls in Fig. 2(a) were all built with fine mesh because of the high-rate turbulence. This type of grid was also used for traffic roundabout and squares, as shown in Fig. 2(b), which represented only 1/4 of the entire roundabout and square.

Before the calculation, tests were conducted by comparing the results obtained from three different mesh systems. Corresponding information appears in Table 2.

To verify grid independence, cases containing the three mesh systems of $U_{ref} = 2$ m/s and θ = 0° were performed, and the results on the Z2 line was plotted in Fig. 3. Equation (13) and (14) explained the error among the three mesh systems, and mesh system B was selected as the standard.

$$E_{B-A} = \frac{|V_A - V_B|}{V_B} * 100\% \tag{13}$$

$$E_{B-C} = \frac{|V_C - V_B|}{V_B} * 100\% \tag{14}$$

where E denotes the error; V is a variate and the subscript; and A, B, and C represent the corresponding mesh systems. The results indicated that the maximal error of these variates was 4.37% (except for the first point on Z2 line near the ground), which was acceptable according to Tominaga et al. (2008) and Franke et al. (2007). Hence, system B was employed in this paper. The maximal y+ value of system B was 7.11, which is fitted with RNG k-ε model.

3. Results and discussion

### 3.1. Influence of wind direction

3.1.1. Bus stop

Fig. 4 shows the streamlines at the sunken bus stop area in different ACWs. Clearly, the velocity decreased as it entered such a low-lying area. In the five cases, vortices emerged regardless of the ACW. The development of vortices and their final shapes exhibited a more uniform characteristic due to the symmetry of the geometrical structure for cases where θ = 0° and θ = 180°. For the case where θ = 90°, the shape of the vortex was oppositely imbalanced, mainly due to the obstruction from the large board at the bus stop. In the cases were θ = 45° and θ = 135°, the shape of the vortices moved along the flow direction and developed in the peripheral wall of this area, and the shape was extremely irregular. Existing studies of the flow field in street canyons have shown the flow field to be mainly affected by the street canyon's aspect ratio, the ladder-type layout of the building, ACW direction, and
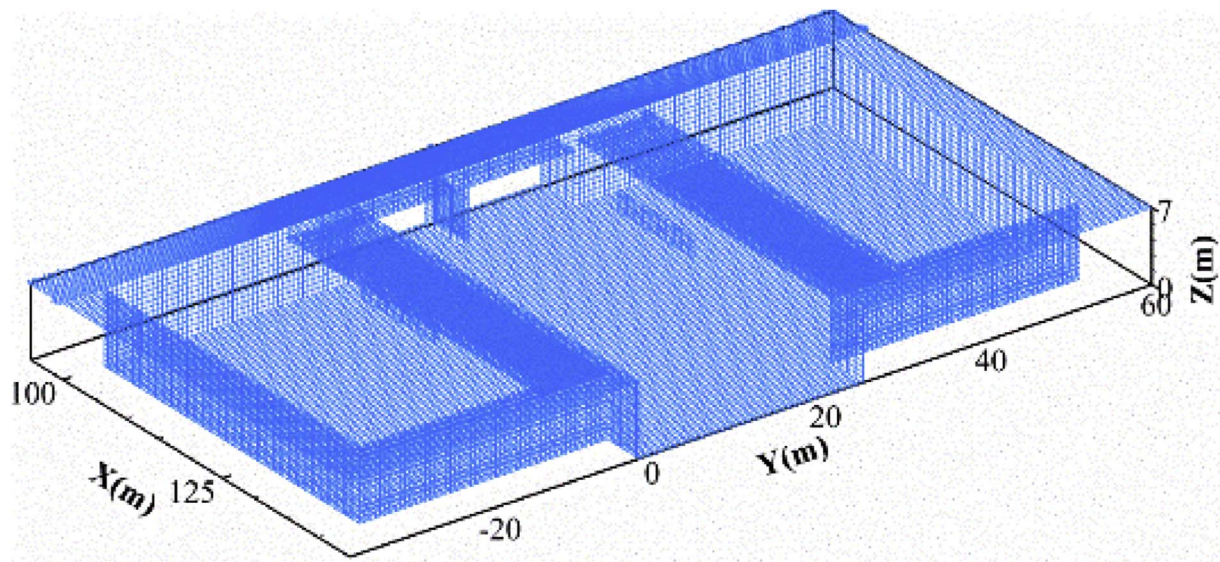
(a)
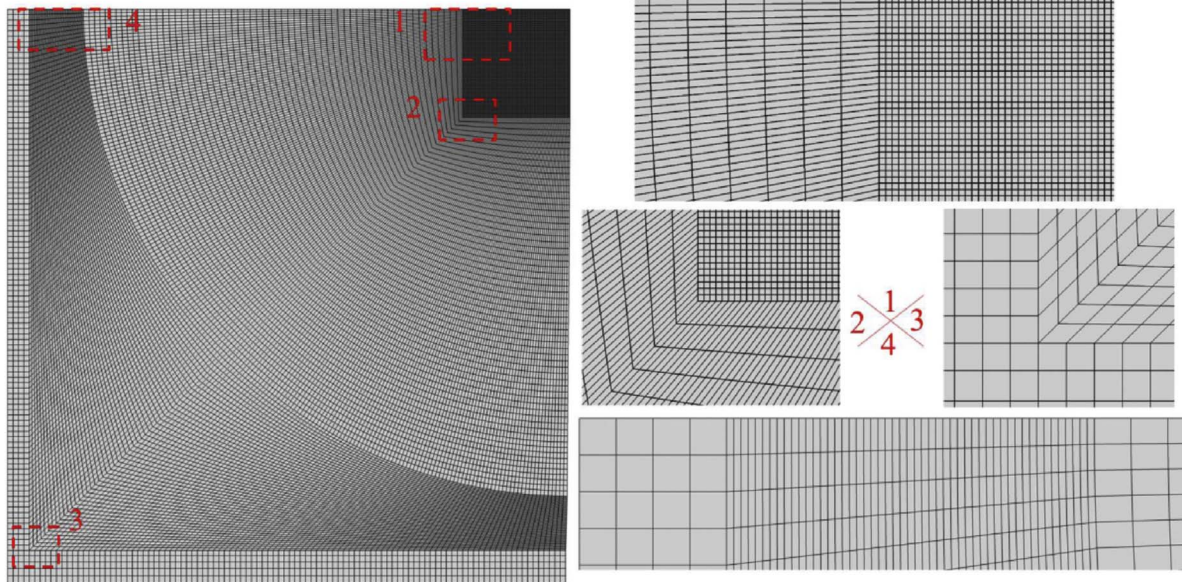
(b)

Fig. 2. Local-area grid of the domain: (a) mesh in bus stop area; (b) mesh in traffic roundabout.

Table 2
Different grid size and numbers of the computational domain.

Mesh system classification	Quality	Minimum grid spacing	Mesh numbers
Mesh system A	coarse	$\delta x_{min} = \delta x_{min} = \delta x_{min} = 0.1H$	6,679,914
Mesh system B	fine	$\delta x_{min} = \delta x_{min} = \delta x_{min} = 0.07H$	7,824,280
Mesh system C	finest	$\delta x_{min} = \delta x_{min} = \delta x_{min} = 0.056H$	9,084,716

the geometric characteristics of the roof (Kastner-Klein and Plate, 1999; Kim and Baik, 2004; Ming et al., 2017). However, the formation of the vortex in such a traffic system is more affected by its complex geometric shape and positional relationship. It was clear in our study that the board hindered the airflow and affected the spread of contaminants. The bus stop area was located between DHTT and an opening underground road on the south side. The asymmetry of the model also caused distribution differences in the flow field under different ACWs.

Compared with other ACWs, airflow was more easily deflected near the board at $\theta = 0°$ and $\theta = 90°$. The deflection was mainly caused by the sudden expansion process when airflow came out of the DHTT in the case where $\theta = 0°$. In the case where $\theta = 180°$, the passage of airflow narrowed when it reached DHTT, causing deflection. Under the cases where $\theta = 45°$ and $\theta = 135°$, the different distribution of the flow field in this area was mainly due to the shape difference of the adjacent structure on the northern and southern sides. At the same time, wind flowed more smoothly into the area when $\theta = 135°$ because of the relationship between the wind direction and the model.

Fig. 4(f) shows the average wind speeds based on the area integral on the cross-section of the viaduct in different ACWs. The velocity was highest below the viaduct located at the western and eastern side when $\theta = 90°$, where the Y-velocity component was most prominent. Because the Y-velocity component was perpendicular to the vertical plane below the viaduct, air circulated easily throughout the entire bus stop area. At the same time, the minimum velocity value occurred when $\theta = 0°$, mainly hindered by the DHTT on the north side. Furthermore, when
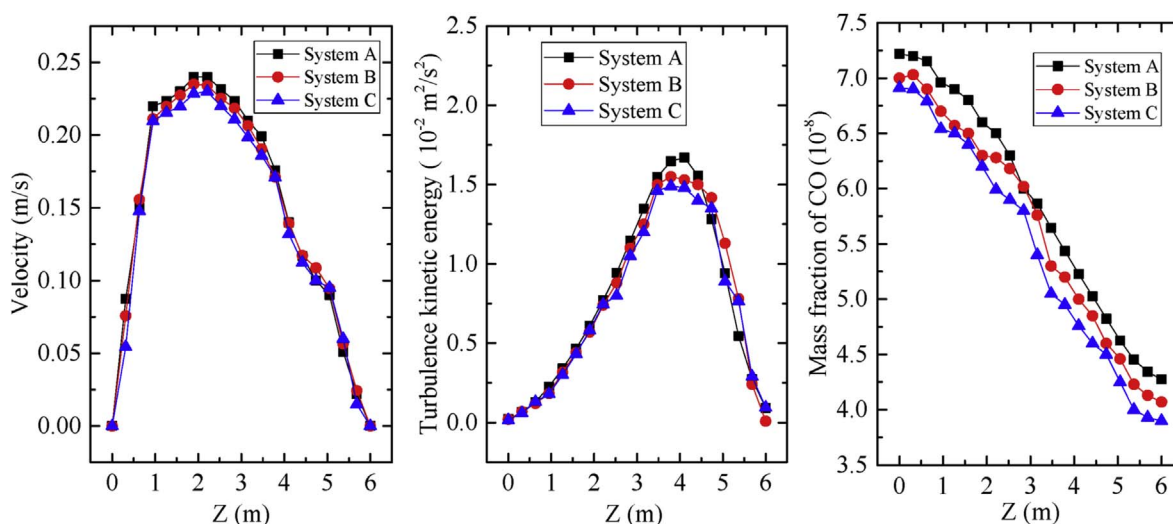
Fig. 3. Comparison of different variates on Z2 line under different mesh systems. (a) velocity; (b) turbulence kinetic energy; (c) mass fraction of CO.

$\theta = 45°$ and $\theta = 135°$, the average wind speed ranged between $\theta = 0°$ and $\theta = 90°$, and the sum of the mean velocity value was $\theta = 135° > \theta = 45°$, which shares the same regulation noted above.

Fig. 5 shows the distribution of the CO mass fraction on the P4 plane. In summary, the symmetry of the geometrical structure also contributed to symmetrical distribution of pollutants in the cases where $\theta = 0°$ and $\theta = 180°$; see Fig. 5(a) and (e).

Fig. 5(f) shows the average mass fraction of CO on planes P2 and P3, and the ACW of $\theta = 0°$ reached the highest level. The main reason for this phenomenon was that pollutants in channels were brought to this area. The same mean mass fraction on P2 and P3 occurring in the cases where $\theta = 0°$ and $\theta = 180°$, respectively, further demonstrates the symmetry of pollutant dispersion in those two ambient wind directions. In the cases where $\theta = 45°$, $\theta = 90°$, and $\theta = 135°$, there was always a relationship between the eastern and the western board: the western board was located in the upstream, and the eastern board was located in the downstream. Therefore, the distribution of pollutants was asymmetric. Except where the contaminant level was higher in the upstream when $\theta = 45°$, the other two cases demonstrated the opposite. Abnormal cases were caused by local airflow, which is explained in Fig. 4. Given the pollutant magnitude of several wind directions in the simulated cases on planes P2 and P3, the relationship was $\theta = 0° > \theta = 45° > \theta = 180° > \theta = 135° > \theta = 90°$. Clearly, $\theta = 90°$ was most favorable for pollutant diffusion in the sunken bus stop area.

3.1.2. Square

Fig. 6 shows the distribution of the CO mass fraction on the P1 plane. In general, pollutant distribution has a direct relationship with wind direction and the position of the pollution source. In our case, pollutant distribution was characterized by symmetrical distribution along wind, except when $\theta = 45°$ and $\theta = 135°$. When $\theta = 0°$, there were two regions with symmetrical distributions of high-level pollutants in the left side of Fig. 6(a) because P1 is in the downstream region of the traffic associated road on the northern side of the model. This same reason also explains the distribution characteristics of $\theta = 180°$, except that the viaduct is in the upstream.

Relatively low pollutant concentration appeared in the cases were $\theta = 45°$, $\theta = 90°$, and $\theta = 135°$ due to the fresh air and lack of pollutant sources in the incoming direction. When $\theta = 90°$, the pollutant distribution exhibited strict symmetry characteristics. If there is a split line through the center of the square along the direction of ACW, contaminant concentration accumulates more on the left side of the dividing line when $\theta = 45°$. Here, the ACW did not match the model's axis; furthermore, a partial pollution source was located on the north

side of the model. Based on the above influence, the pollutants were transported to this area, forming Fig. 6(b). This is similar to the explanation for Fig. 6(d), except that the pollutant source on the viaduct was in the upstream area, resulting in a higher-level area on the right top side. This also explains why the mean level of $\theta = 45°$ and $\theta = 135°$ is higher than $\theta = 90°$ in Fig. 6(f).

Among the five cases in Fig. 6(f), $\theta = 180°$ contributes the highest; here, the air flowed through the sunken area and deflected upward. Because the longer lane in the south part of the P1 plane provided more pollution, the airflow with more contaminants diffused into this area and increased the pollutant level. Upward airflow also occurred when $\theta = 0°$, but the lane on the north side was short, resulting in less pollution at the lower level compared with $\theta = 180°$. It can be concluded that the effect of complex road conditions on pollutant dispersion is beyond the effect of ACW directions at the roundabout. Suresh (Pandian et al., 2011) argued that the complex distribution of traffic roads at roundabouts had a higher impact on pollutant dispersion than the prevailing wind, echoing the results of this study.

3.2. Influence of wind velocity

3.2.1. Bus stop

Due to the bus stop boards, the blocking effect cannot be ignored, especially for the ACW perpendicular to them. Fig. 7 shows the flow chart of plane P4. It can be seen that two vortices formed on the western and eastern side of the bus stop. The airflow, blocked by the board, passed through the area obscured by the board. In comparison, the scale of the downwind vortex was larger, and the vortex stayed closer to the wall as ACW increased. The scenario is similar to the structure of the street canyon, where the region will only form a larger vortex (Zhong et al., 2015). In our study, the vortex was cut off by viaducts and bus stops, resulting in the formation of two vortices, one large and one small. It can be concluded that the geometric characteristics of complex 3D traffic severely affected the distribution of its flow field, which is more complicated than a single-channel flow field in a street canyon.

The vertical velocity near the viaduct was small enough to be ignored. The airflow leaving the space below the western viaduct (SBWV) could be divided into three parts: 1) direct flow into the space below the eastern viaduct (SBEV), defined as Q1; 2) flows into the western and eastern tunnel (if any), defined as Q2; and 3) flow into the opening traffic road underground on the southern side attached to the sunken zone, defined as Q3. The flow into SBEV could also be divided into three parts: 1) the direct flow rate from the SBWV, defined as Q4; 2) the flow from the space attaching above the western viaduct, defined as Q5;
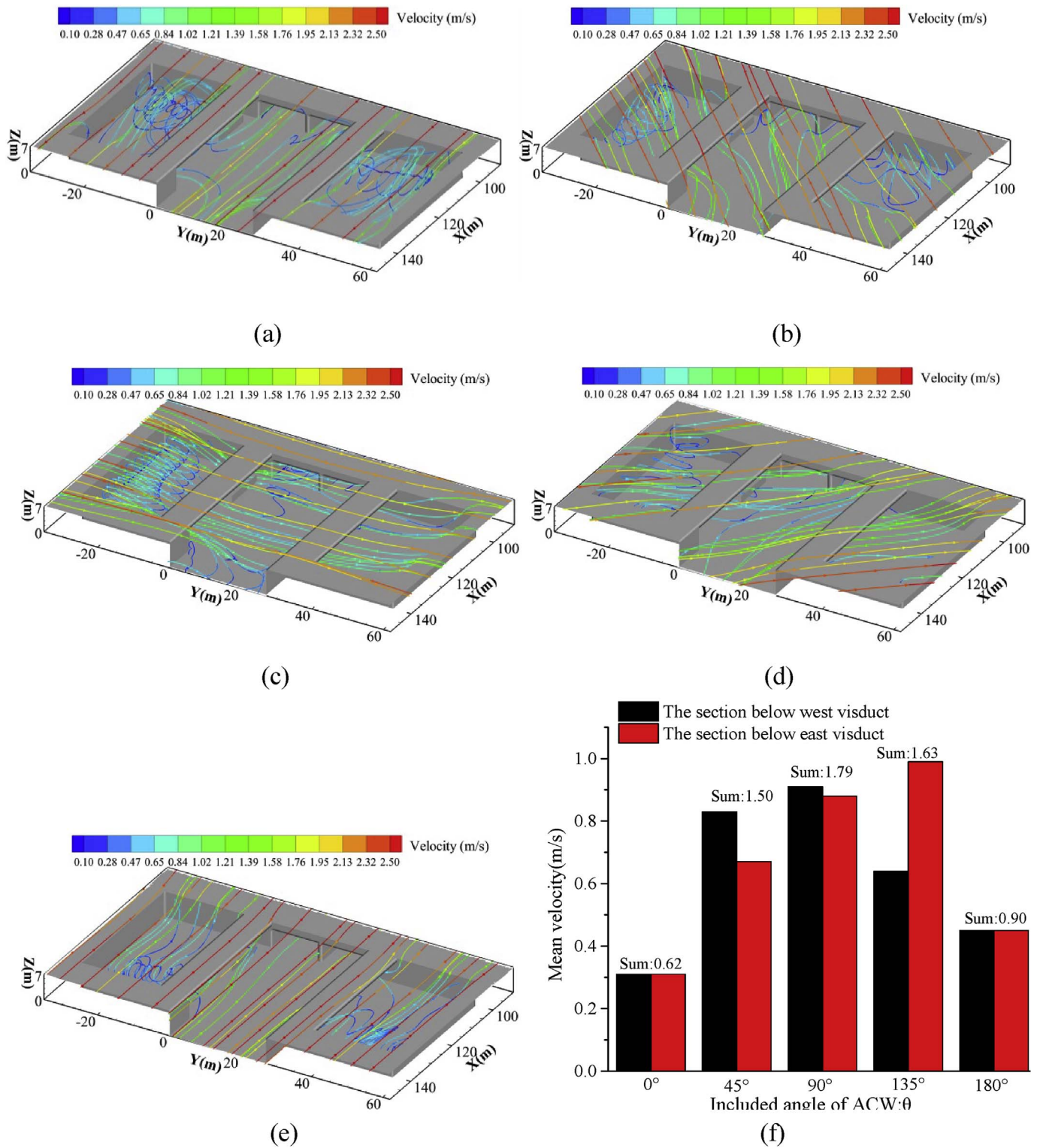
Fig. 4. Flow chart of the bus stop area with different wind directions for ACW = 2.0 m/s: (a) θ = 0°; (b) θ = 45°; (c) θ = 90°; (d) θ = 135°; (e) θ = 180°; (f) The average velocity flows through the space below the western viaduct.

and 3) the flow (if any) from the eastern tunnel, defined as Q6. Although the specific values of these subjects may not be clear, they are of great help for analyzing streams in this area. It is not difficult to see that Q1 and Q4 are always equal, and the flow rate through SBWV and SBEV can be analyzed via the other objects mentioned above. Consequently, we obtained the area-weighted average velocity in both positions; simulation results are shown in Fig. 8.

The results indicated that airflow traveled from south to north in the west tunnel, while it traveled in the opposite direction in the east tunnel. In addition Q2 > Q6. Fig. 7 shows that the mean velocity of the SBWV was higher than that of SBEV; thus, Q2 + Q3 > Q5 + Q6.

Fig. 9 shows the distribution of the CO mass fraction on the P4 plane at different ambient wind speeds. First, it is clear that a larger ACW results in smaller CO mass fractions. Second, the concentration at the

(a)

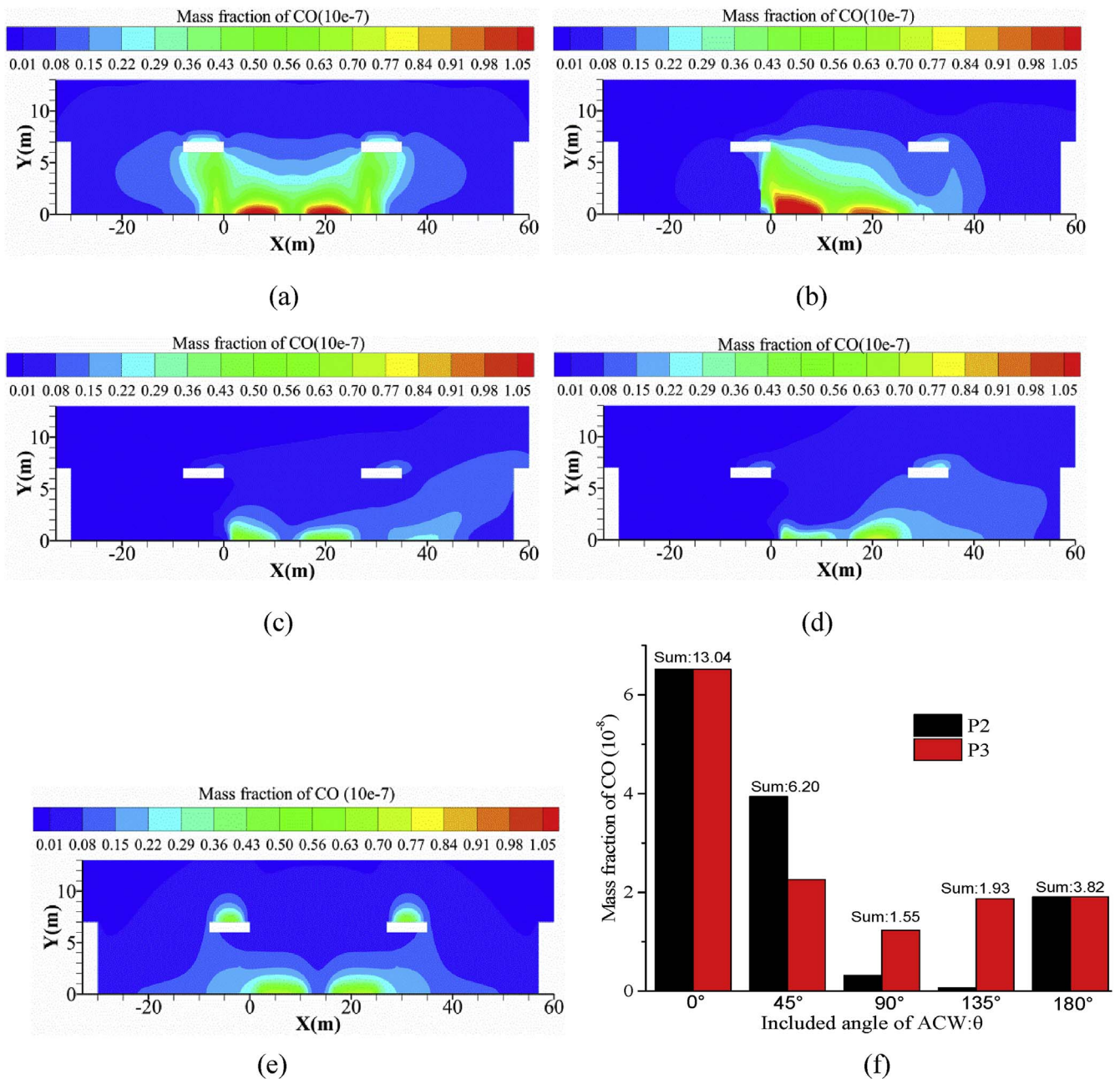(b)

(c)

(d)

(e)

(f)

Fig. 5. Distribution of the CO mass fraction on the P4 plane of different ambient winds and the histogram of average CO mass fraction on P2 and P3 when ACW = 2.0 m/s: (a) θ = 0°; (b) θ = 45°; (c) θ = 90°; (d) θ = 135°; (e) θ = 180°; (f) Average mass fraction of CO on P2 and P3.

eastern board was much larger than that at the western board when θ = 90°, presumably due to incoming fresh air and its efficient dilution effect; however, the pollutants migrated with the air downstream to the eastern board. The airflow, on one hand, diluted the contaminants, although the concentration increased within itself at the same time. The relatively high pollutant levels between the two boards were mainly due to poor air circulation, which can be seen more clearly in Fig. 7. The mass fraction of the CO gradient was significantly smaller along the horizontal direction than the vertical, which indicates that contaminants spread easily along the vertical direction.

Fig. 10 shows the CO mass fraction curves on the Z1 and Z2 lines. The transport of the contaminants at this position depended mainly on the wind, and the CO level decreased as wind speed increased. Fig. 10(a) shows the peak caused by the west board. There was a low-speed zone behind the board along the flow caused by the reversed flow. The zone decreased ventilation, making it difficult for

contaminant to migrate, resulting in the pollutant peak. Away from the board, whether up or down, the airflow velocity increased with distance from the barrier. Therefore, the line moved down from the peak to both sides. In addition, the areas close to the ground showed higher pollutant levels than those below the viaduct given their distance from pollutant source.

Fig. 10(b) shows the distribution of the CO mass fraction on the Z2 line. The pollutant concentration decreased with height, mainly because of the high velocity there. This change trend differed from Z1; the rate of change was also larger than on the west side. It was relatively smooth, coinciding with research from Ramponi et al. (Defraeye et al., 2012), who believed that weaker obstruction effects occurred downwind along the flow direction.

3.2.2. Traffic tunnel

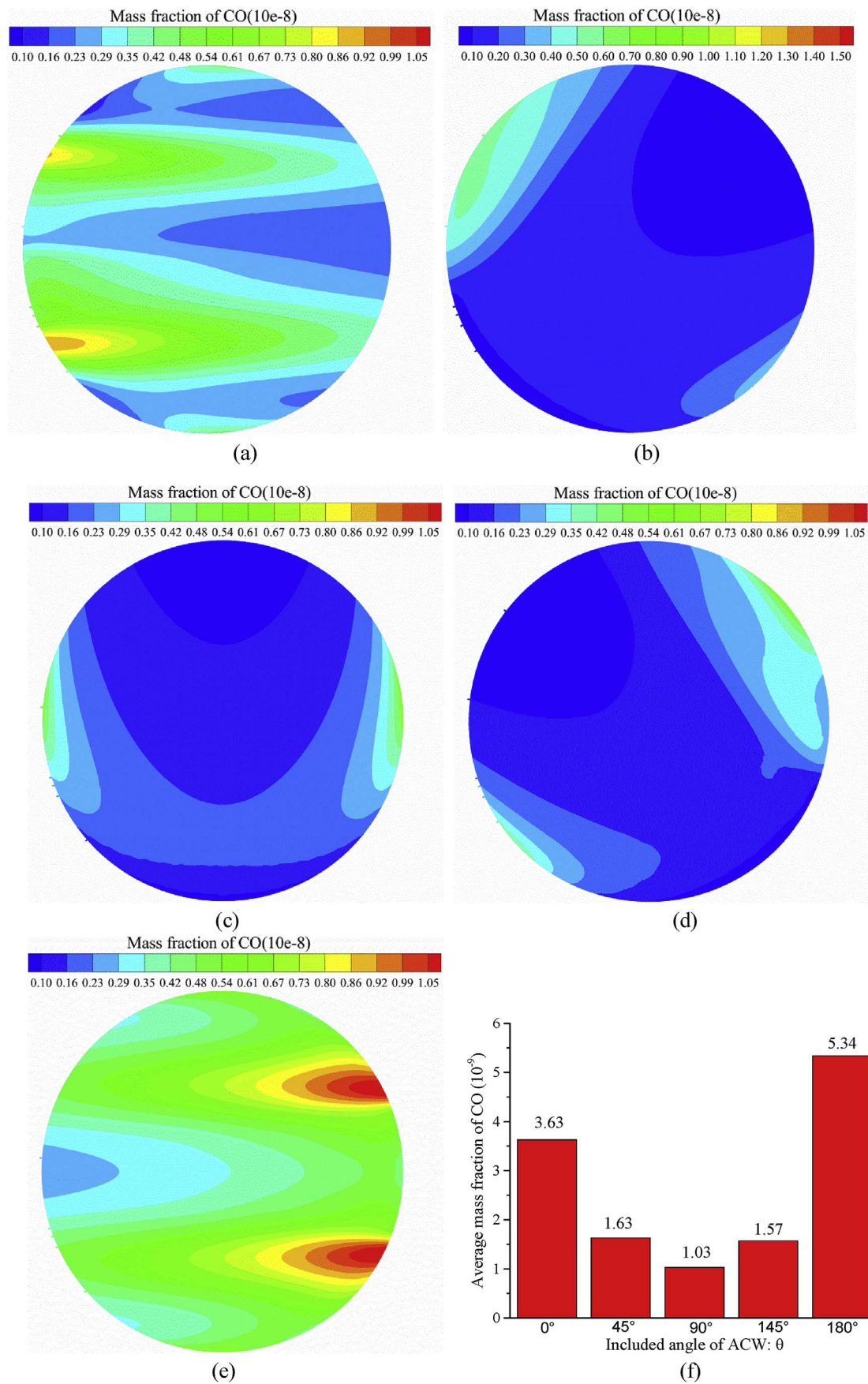Fig. 11 indicates the distribution of CO mass fraction on X1 and X2.

Fig. 6. Distribution of the CO mass fraction and its histogram of average fraction in the P1 plane of different ambient wind directions when ACW = 2.0 m/s: (a) θ = 0°; (b) θ = 45°; (c) θ = 90°; (d) θ = 135°; (e) θ = 180°; (f) histogram of the average mass fraction of CO on P1.
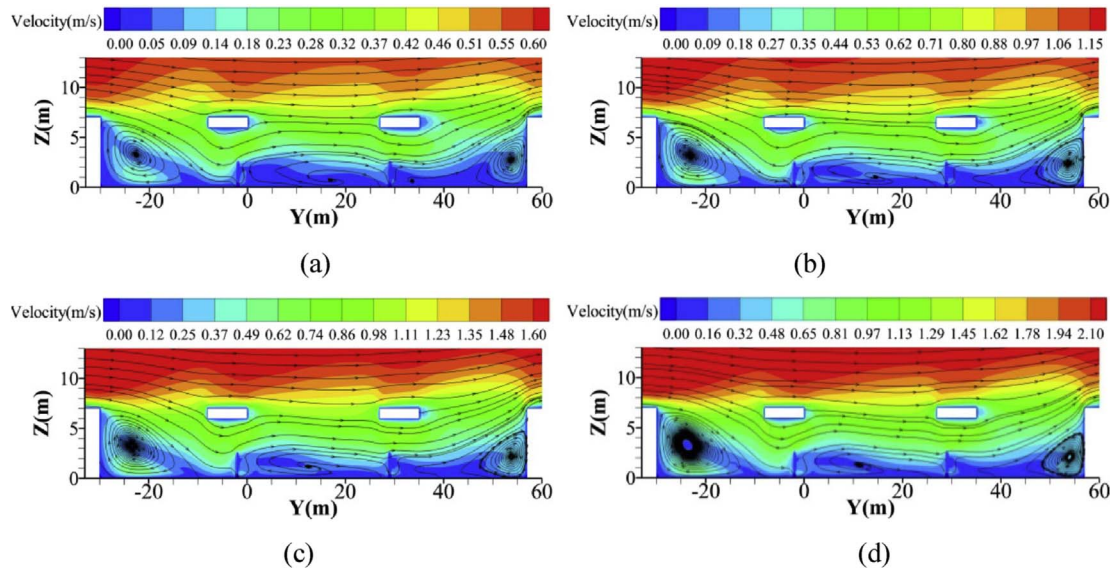
Fig. 7. Streamline chart of the P4 plane and distribution of the Y-velocity component under different ambient wind velocities: (a) U_{ref} = 0.5 m/s; (b) U_{ref} = 1.0 m/s; (c) U_{ref} = 1.5 m/s; (d) U_{ref} = 2.0 m/s.
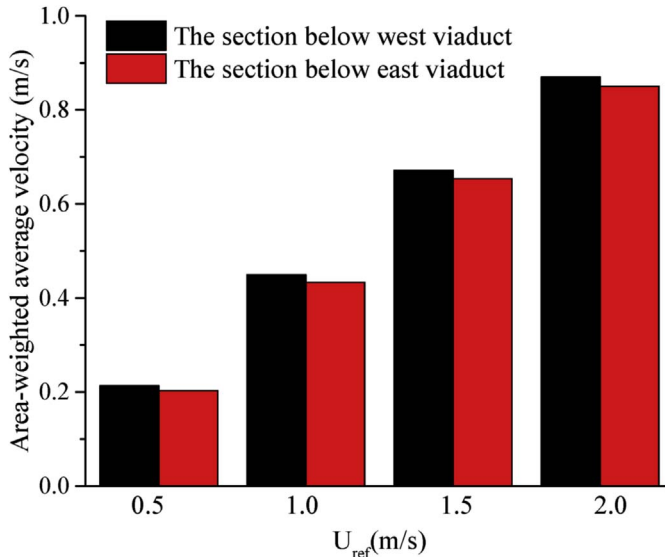

Fig. 8. The average wind speed flowing through the space below the western and eastern viaducts under different environmental wind velocities.

It can be concluded that the CO level decreased with increasing ACW at the fixed position. Pollutants migrating to one direction in this type of closed tunnel will inevitably accumulate downstream, which aligned with the research of Chen and Chung. (Chen et al., 2002; Chung and Chung, 2007). Apparently, peaks occurred in the northern half of the west tunnel and in the southern half of the east tunnel.

The distribution of pollutants on the X1 peaks and higher ACW brought pollutants closer to the northern end of the tunnel. This hump-like feature was more pronounced when U_{ref} = 0.5 m/s. Simulation results showed that the current in the west tunnel flowed from south to north, which is why the peak appeared in the northern half of the tunnel. Fig. 10(a) indicates that the mass fraction of CO at the opening area was 7.22×10^{-8}, while the peak concentration was 1.54×10^{-6}, constituting a 21.3-fold increase estimated via the result of U_{ref} = 0.5 m/s. While the value was 1.81×10^{-8} at the opening area, the peak occurred at 1.89×10^{-7}, a 10.4-fold increase for ACW = 2.0 m/s. It is clear that the accumulation effect was more obvious at a low ambient velocity and the pollutant level in the opening

area was lower, similar to the east tunnel.

The trend of pollutants on the X2 line also showed a hump-like feature due to the accumulation effect. In fact, pollutant formed a peak in the southern half of the east tunnel. Results has indicated that airflow direction in the east tunnel is opposite from the west. The same trend appeared in both tunnels (i.e., the pollutant level decreased as U_{ref} increased). The pollutant level on the X2 line was slightly higher in the case of U_{ref} = 1.5 m/s compared to U_{ref} = 2.0 m/s, which is an unusual difference. The mean velocity in the tunnel, as shown from the results, was 10.2% more in the case of U_{ref} = 1.5 m/s than U_{ref} = 2.0 m/s, which illustrates the identified phenomenon. Naturally ventilated tunnels have come to play an increasingly important role in modern cities, and the characteristics of pollutant dispersion in this type of tunnel will be the subject of research in our next study.

4. Discussion

With the continuous deepening of China's urbanization process, skyscrapers and complex traffic systems are blooming greatly in Chinse metropolises. The traffic systems with the combination of viaducts, tunnels, and roundabout become a typical structure in modern Chinse metropolises to alleviate the transportation pressure. However, bus stops are generally built under the viaducts or the exits of tunnels in urban design, where the issue concerning the passengers' health in the bus stops has generally been ignored.

Thereby, the results of the study will provide some suggestions to traffic design-makers or traffic managers. It is strongly recommended that the bus stops should be moved to open area far away from the entrance and exits of tunnels. Besides, traffic managers should warm the people to decrease outdoor activities properly in squares bounded by complex traffic lanes, when traffic jam happens.

5. Conclusions

In this study, a numerical simulation method was utilized to explore gaseous pollutant dispersion in a three-dimensional traffic system. Considering various directions and velocities of ambient wind, the following conclusions were drawn from our analysis.

(1) In contrast to general traffic and building characteristics with a single structure, the pollutant dispersion in 3D traffic is more constrained by the geometric characteristics of the traffic system and
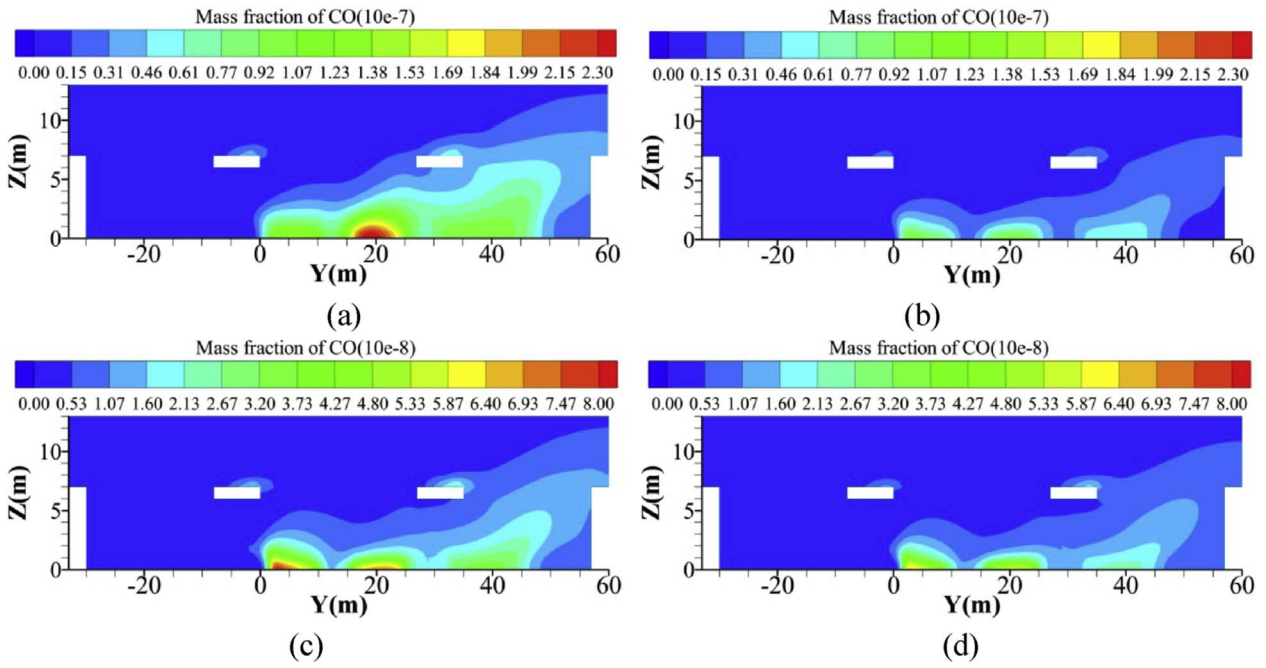
Fig. 9. Distribution of mass fraction of the CO on the P4 plane at different ambient wind velocities: (a) ACW = 0.5 m/s; (b) ACW = 1.0 m/s; (c) ACW = 1.5 m/s; (d) ACW = 2.0 m/s.
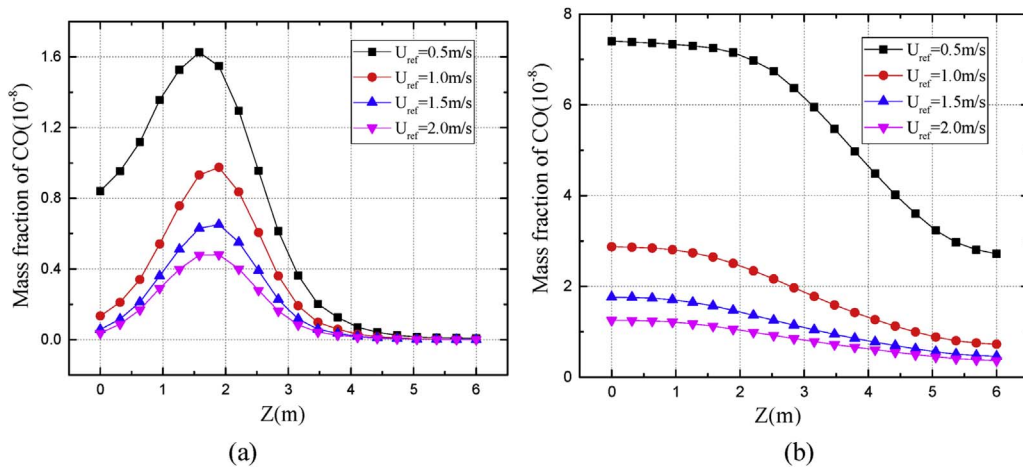

Fig. 10. Curves of mass fraction of CO at different wind velocities on lines Z1 and Z2: (a) Z1 line; (b) Z2 line.
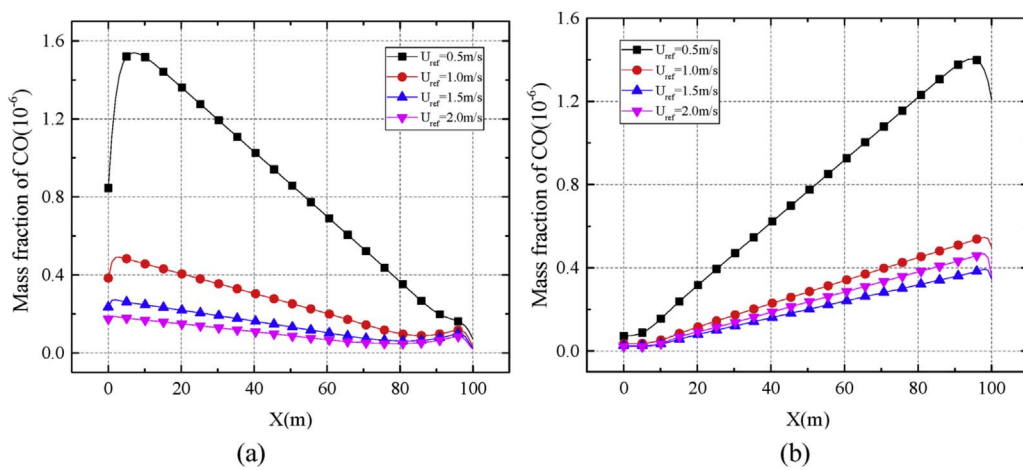

Fig. 11. Curves of mass fraction of CO at different wind velocities on lines X1 and X2: (a) X1 line; (b) X2 line.

their positional relationship. In the sunken bus stop region, the bus stop board severely hampered the surrounding airflow. Influenced by the geometric characteristics of the surrounding structures, more pollutants were transported to the bus stop area from poorly ventilated tunnels where contaminants are more concentrated.

(2) In the obstacle-free square, the pollutants showed a symmetrical distribution along the wind direction, while the position of the pollution source also caused high local pollution levels. The impact of the complex distribution of traffic on pollutant dispersion at the traffic roundabout went beyond the prevailing wind direction.

(3) Pollutants accumulated in the downstream area, and this phenomenon was more pronounced in the case of low ACW in naturally ventilated tunnels. At the same time, velocity increased near the opening, leading to a low pollutant level there.

References

Chen, K.S., Chung, C.Y., Wang, S.W., 2002. Measurement and three-dimensional modeling of airflow and pollutant dispersion in an undersea traffic tunnel. J. Air Waste Manag. Assoc. 52 (3), 349.

Chung, C.Y., Chung, P.L., 2007. A numerical and experimental study of pollutant dispersion in a traffic tunnel. Environ. Monit. Assess. 130 (1–3), 289–299.

Cussler, E.L., 1986. Diffusion, mass transfer in fluid system. Cambridge University Press, NewYork, pp. 17–25.

De_Richter, R., Ming, T., Davies, P., Liu, W., Caillol, S., 2017. Removal of non-CO_2 greenhouse gases by large-scale atmospheric solar photocatalysis. Prog. Energy Combust. Sci. 6068–6096.

Defraeye, T., Blocken, B., Carmeliet, J., 2012. CFD simulation of heat transfer at surfaces of bluff bodies in turbulent boundary layers: evaluation of a forced-convective temperature wall function for mixed convection. J. Wind Eng. Ind. Aerodyn. 104–106 (3), 439–446.

FLUENT, V., 2006. User's manual. http://www.fluent.com2006.

Franke, J., Hellsten, A., Schlünzen, H., Carissimo, B., 2007. Best Practice Guideline for the CFD Simulation of Flows in the Urban Environment. Cost Office Brussels 732. .

Gokhale, S., Patil, R., 2010. Uncertainty in modelling PM 10 and PM 2.5 at a non-signalized traffic roundabout. Atmos. Pollut. Res. 1 (2), 59–70.

Hang, J., Lin, M., Wong, D.C., Wang, X., Wang, B., Buccolieri, R., 2016. On the influence of viaduct and ground heating on pollutant dispersion in 2D street canyons and toward single-sided ventilated buildings. Atmos. Pollut. Res 7 (5), 817–832.

Kastner-Klein, P., Plate, E.J., 1999. Wind-tunnel study of concentration fields in street canyons. AtmEn 33 (24–25), 3973–3979.

Kim, J.J., Baik, J.J., 2004. A numerical study of the effects of ambient wind direction on flow and dispersion in urban street canyons using the RNG – turbulence model. AtmEn 38 (19), 3039–3048.

Konstantinov, A., Staroselsky, I., Orszag, S.A., Yakhot, V., 1998. Renormalization group-based transport modeling of premixed turbulent combustion: I. Incompressible deflagration model. JSCom 13 (3), 229–252.

Krecl, P., Targino, A.C., Johansson, C., Ström, J., 2015. Characterisation and source apportionment of submicron particle number size distributions in a busy street canyon. Aerosol. Air Qual. Res. 15 (1), 220–233.

Lin, M., Wong, D.C., Li, Y., Hang, J., 2014. The Influence of Viaduct and Ground Heating on Pollutant Dispersion within Street Canyons and from Outdoor to Indoor: Gaseous Pollutant and Particle Simulations. pp. 580–587.

Liu, Y., Lu, S.S., Chang, C.C., Wang, J.L., Fu, L., 2008. Source apportionment of ambient volatile organic compounds in the Pearl River Delta, China: Part II. AtmEn 42 (25), 6261–6274.

Long, T., 2007. Computational Fluid Dynamics. Chongqing University Press.

Lu, C., Deng, L., Ou, C., Yuan, H., Chen, X., Deng, Q., 2017. Preconceptional and perinatal exposure to traffic-related air pollution and eczema in preschool children. J. Dermatol. Sci. 85 (2), 85–95.

Mcdonald, J.D., Eide, I., Seagrave, J.C., Zielinska, B., Whitney, K., Lawson, D.R., Mauderly, J.L., 2004. Relationship between composition and toxicity of motor vehicle emission samples. Environ. Health Perspect. 112 (15), 1527.

Ming, T., Gong, T., Peng, C., Li, Z., 2017. Pollutant Dispersion in Built Environment. Springer, Singapore.

Moradpour, M., Afshin, H., Farhanieh, B., 2016. A numerical investigation of reactive air pollutant dispersion in urban street canyons with tree planting. Atmos. Pollut. Res. 8 (2), 253–266.

Moradpour, M., Afshin, H., Farhanieh, B., 2017. A numerical study of reactive pollutant dispersion in street canyons with green roofs. Build. Simul. 1–14.

National Bureau of Statistics of China, 2017. National Bureau of Statistics of China. http://data.stats.gov.cn/, Accessed date: 1 October 2017.

Pandian, S., Gokhale, S., Ghoshal, A.K., 2011. An open-terrain line source model coupled with street-canyon effects to forecast carbon monoxide at traffic roundabout. ScTEn 409 (6), 1145–1153.

Patankar, S.V., 1980. Numerical Heat Transfer and Fluid Flow.

Raw, M.R., Galpin, P.F., Hutchinson, B.R., 1989. A co-located finite volume method for solving the Navier-Stokes equations for incompressible and compressible flows in turbomachinery - results and applications (Le Journal Aéronautique Et Spatial Du Canada). Can. Aeronaut. Space J. 35 (4), 189–196.

Richards, P.J., Hoxey, R.P., 1993. Appropriate boundary conditions for computational wind engineering models using the k-ε turbulence model. J. Wind Eng. Ind. Aerodyn. 46–47 (93), 145–153.

Richards, P.J., Norris, S.E., 2011. Appropriate boundary conditions for computational wind engineering models revisited. J. Wind Eng. Ind. Aerodyn. 99 (4), 257–266.

Sabatino, S.D., Buccolieri, R., Salizzoni, P., 2013. Recent advancements in numerical modelling of flow and dispersion in urban areas: a short review. Int. J. Environ. Pollut. 52 (3–4), 172–191.

Scungio, M., 2013. Numerical simulation of ultrafine particle dispersion in urban street canyons with the spalart-allmaras turbulence model. Aerosol Air Q. Res. 13 (5), 1423–1437.

Scungio, M., Arpino, F., Cortellessa, G., Buonanno, G., 2015a. Detached eddy simulation of turbulent flow in isolated street canyons of different aspect ratios. Atmos. Pollut. Res. 6 (2), 351–364.

Scungio, M., Buonanno, G., Arpino, F., Ficco, G., 2015b. Influential parameters on ultrafine particle concentration downwind at waste-to-energy plants. Waste Manag. 38 (1), 157–163.

Shahbazi, H., Reyhanian, M., Hosseini, V., Afshin, H., 2016. The relative contributions of mobile sources to air pollutant emissions in tehran, Iran: an emission inventory approach. Emiss. Control Sci. Technol. 2 (1), 44–56.

Solazzo, E., Cai, X., Vardoulakis, S., 2008. Modelling wind flow and vehicle-induced turbulence in urban streets. AtmEn 42 (20), 4918–4931.

Soulhac, L., Garbero, V., Salizzoni, P., Mejean, P., Perkins, R.J., 2009. Flow and dispersion in street intersections. AtmEn 43 (18), 2981–2996.

Tang, T., Roberts, M., Ho, C., 2003. Sensitivity Analysis of Mobile6 Motor Vehicle Emission Factor Model.

Tominaga, Y., Mochida, A., Yoshie, R., Kataoka, H., Nozu, T., Yoshikawa, M., Shirasawa, T., 2008. AIJ guidelines for practical applications of CFD to pedestrian wind environment around buildings. J. Wind. Eng. Ind. Aerodyn. 96 (10), 1749–1761.

Tsai, M.Y., Chen, K.S., 2004. Measurements and three-dimensional modeling of air pollutant dispersion in an Urban Street Canyon. AtmEn 38 (35), 5911–5924.

Zhang, Y.W., Gu, Z.L., Lee, S.C., Fu, T.M., Ho, K.F., 2011. Numerical simulation and in situ investigation of fine particle dispersion in an actual deep street canyon in Hong Kong. Indoor Built Environ. 20 (2), 206–216.

Zhong, J., Cai, X.M., Bloss, W.J., 2015. Modelling the dispersion and transport of reactive pollutants in a deep urban street canyon: using large-eddy simulation. Environ. Pollut. 20042.